DOI: https://doi.org/10.37434/tpwj2025.09.03

MATHEMATICAL MODELING OF HEAT AND MASS TRANSFER PROCESSES DURING ELECTRON BEAM MELTING OF Ti–6Al–Nb TITANIUM ALLOY INGOTS

I.V. Krivtsun, S.V. Rymar, R.S. Gubatyuk, V.O. Berezos, D.S. Akhonin, R.V. Selin

E.O. Paton Electric Welding Institute of the NASU
11 Kazymyr Malevych Str., 03150, Kyiv, Ukraine

ABSTRACT

The results of mathematical modeling of temperature fields and hydrodynamic laminar flows of the liquid metal during electron beam melting of titanium alloy ingots are presented. The calculations were performed using the developed three-dimensional mathematical model based on the finite element method taking into account a number of simplifications and assumptions. The model allows determining the regularities of thermal and hydrodynamic processes occurring in a continuous water-cooled mould during ingot melting, and the geometry of the liquidus-solidus interphase transition zone, and accordingly, of the metal crystallization front, which significantly affects the quality of the metal during ingot formation. We calculated the parameters of the melting process for ingots of a small diameter of 110 mm from the medical Ti–6Al–7Nb titanium alloy with such a crystallization front, for which the production of high-quality metal with a homogeneous structure and a homogeneous distribution of alloying elements in the ingot volume is ensured. It was found that the heat and mass transfer in the liquid metal is significantly affected by the power of the electron beam and its distribution over the pool surface, and the heat transfer is mainly predetermined by the movement of the melt.

KEYWORDS: electron beam melting, titanium alloys, mathematical modeling, heat and mass transfer, metal crystallization front

INTRODUCTION

Light, strong, biocompatible, and non-toxic implants and endoprostheses made of metals and special alloys for medical long-term use are widely used in surgery. About 60 % of the market is occupied by implants made of metal, and titanium and its alloys are the leaders among these products [1], since their strength is equal to that of cobalt alloys, exceeds that of stainless steels, and has a modulus of elasticity that is twice lower (55–112 GPa), while that of chromium-cobalt alloy is 240 GPa and that of chromium-nickel stainless steels is 210 GPa. Such a low elasticity index is extremely important for joint and bone endoprostheses and implants, as it is closer to the indices of human bones, where it is 27.8–30.0 GPa in the longitudinal direction and 11.0–11.5 GPa in the radial and azimuthal directions.

The corrosion-resistant low-toxicity [2] Ti–6Al–4V alloy is widely used in medicine, as it surpasses stainless steels and cobalt alloys in terms of biological compatibility. Ti–6Al–4V alloy contains an order of magnitude less hazardous vanadium (4 % by weight) compared to stainless steels, in which the mass concentration of toxic nickel and chromium exceeds 30 %.

In modern metallurgy, there is a task to improve the technology for melting the latest medical titanium alloys without toxic alloying elements. At present, these are the latest titanium alloys with niobium, niobium and zirconium, and molybdenum and zirconium, which are close in their mechanical properties to Ti–6Al–4V alloy [3]. The alloys are non-toxic to the human body and have excellent biological compatibility, corrosion resistance, and ductility. Thus, the elastic modulus of Ti–6Al–7Nb alloy is less than 40 GPa.

In the future, titanium alloys may replace stainless steel and cobalt alloys in prosthetics, and surface modification of products, such as mechanical, thermal, cryogenic, electroerosion, chemical treatment, spraying, etc., further improve the modulus of elasticity, corrosion and wear resistance, reduce ion release to prevent inflammation, enhance antibacterial properties, biocompatibility, and adhesion [4–11].

The E.O. Paton Electric Welding Institute of the NAS of Ukraine (PWI) has developed electron beam melting (EBM) technology for the production of defect-free, high-quality titanium alloy ingots with a guaranteed chemical composition, including those for medical use.

One of the key factors affecting the quality of melting titanium alloy ingots is metal crystallization. The transformation of metal from a liquid to a solid state is accompanied by complex heat and mass transfer processes and rapid physical and chemical processes. The uneven temperature field in the volume of the metal ingot affects the formation of the crystallization front profile and leads to differences in the structure and chemical composition of the metal at the center and periphery of the ingot, the presence of shrinkage and liquation phenomena, etc. This significantly affects the quality of the final structure of the metal ingots.

Conducting full-scale experiments of metallurgical processes is associated with significant material

costs, which determines the prospects for using CFD modeling (CFD — Computational Fluid Dynamics) of high-temperature heat and mass transfer processes. Based on a small amount of experimental data, numerical modeling with significantly lower material costs allows calculating and obtaining, with sufficient accuracy for practical use, predicted qualitative and quantitative pictures of the phenomena occurring during metallurgical processes.

Numerical calculation methods and modern computer packages for mathematical modeling allow using thermophysical indices in the form of approximation functions of temperature, which significantly brings calculations closer to real processes.

Knowledge of heat and mass transfer processes in high-temperature melts of titanium alloys during their EBM and ingot formation is a relevant task in modern metallurgy. Knowledge of the shape of the metal crystallization front is one of the key factors in selecting technological modes for melting high-quality ingots. A homogeneous structure and uniform distribution of alloying elements in the ingot is ensured in the case of a flatter crystallization front, resulting in a more uniform temperature distribution in the ingot, which is a prerequisite for obtaining a homogeneous metal structure.

The aim of the work is to perform mathematical modeling of thermal and hydrodynamic processes of EBM of a cylindrical ingot with a diameter of 110 mm made of titanium Ti–6Al–7Nb alloy with a mass withdrawal rate of 20 kg/h, identifying the main regularities of heat and mass transfer processes during melting and determining the necessary melting modes. For this purpose, the following tasks must be solved: develop a mathematical model for calculating thermal and hydrodynamic processes in the ingot in the case of laminar flow of the liquid metal; take into account the thermophysical characteristics of the metal with their change in interphase transition zones; calculate the distribution of temperature fields in the ingot and laminar hydrodynamic flows in the melt pool, and, accordingly, the shape of the metal crystallization profile.

Achieving this aim will make it possible to determine the key technological parameters for melting ingots, which is a relevant issue in the computational search for the necessary melting process modes, excluding extremely costly full-scale experiments.

RESEARCH MATERIALS AND METHODS

The object of study in the work is a mathematical model of heat and mass transfer processes in EBM of titanium alloy ingot. The subject of study is the characteristics of hydrodynamic flows in the melt and temperature fields in the ingot.

The main hypotheses of the research are as follows: representation of the nature of moving hydrodynamic flows of the liquid metal as laminar will provide a result closer to the actual metal crystallization profile than its turbulent representation [12]; the position of the electron beam on the surface of the melt pool, its power, and the rate of ingot withdrawal are the factors that mainly influence the shape of the metal crystallization front and, accordingly, the quality of the metal in the ingot.

The following assumptions were made during the work: the liquid and solid phases of the metal ingot are considered as a single region with a liquid phase, while the solid metal corresponds to the volume in which movement is artificially suppressed by the Darcy braking force (except for the ingot's withdrawal rate) and a fixed calculation mesh is used in the finite element method; the liquidus-solidus (L–S) interphase boundary of the alloy represents a viscous transition zone in which the boundaries are determined by the liquidus and solidus temperatures, and the metal parameters change according to the proposed law relative to the volume fraction of these phases; the volume fraction of the metal in the transition zone as a function of temperature is a smoothed $F_{L–S}$ function that smoothly changes from 0 to 1, using the mathematical error function erf; approximate dependencies of the thermophysical parameters of Ti–6Al–4V and Ti–6Al–7Nb titanium alloys with smoothed stepwise phase transitions are used, applying the erf function with artificially extended temperature limits in phase transitions [13]; the distribution of the electron beam thermal power across the surface of the pool mirror varies according to the Gaussian law; since the lines of metal crystallization profiles are not visually traceable in the melt of the studied Ti–6Al–7Nb alloy, the experimental determination of these profiles was carried out on an experimental titanium alloy with similar physical properties, in which the crystallization profiles are clearly expressed.

The following simplifications are accepted: liquid metal is poured into the mould continuously at the constant rate and a constant rate of ingot withdrawal is ensured, which allows the problem to be considered as a stationary process; the mirror of the melt pool is a flat surface; the molten metal is assumed to be an incompressible viscous liquid; the heat capacity in the α–β and *L–S* phase transition zones of the alloy takes into account the equivalent heat capacity and the heat capacity from the latent heat of phase transitions; evaporation losses from the melt surface take into account only the evaporation of titanium.

The mathematical model uses the fundamental laws of conservation of energy, momentum, and mass, as well as the corresponding heat and mass transfer equations based on the Fourier and Navier–Stokes equations. The finite element numerical method was used for calculations. The ingots were melted using research equipment at the PWI [14–16].

The article is a continuation of research published by the authors in their work [12].

The originality of the work lies in the fact that, for the first time, research has been conducted on the laminar nature of melt flow for a selected mould diameter and the rate of Ti–6Al–7Nb alloy ingot withdrawal in the EBM process.

The practical significance of the work lies in the melting of high-quality titanium alloy ingots with a homogeneous metal structure.

RESEARCH RESULTS

MATHEMATICAL MODEL OF THERMAL AND HYDRODYNAMIC PROCESSES IN A CYLINDRICAL INGOT IN THE CASE OF LAMINAR METAL MELT FLOW

Let us write down the basic equations [12, 17–19] used in the model. The Fourier heat transfer equation in the case of laminar flow of the liquid metal for a stationary process is written as [18, 20, 21]:

$$\rho C_p \mathbf{u} \cdot \nabla T + \nabla \cdot \mathbf{q} = 0; \; \mathbf{q} = -\lambda \nabla T,$$

where ρ is the density of the metal, kg/m^3; C_p is the specific heat capacity of the metal, J/(kg·K); **u** is the velocity vector of the metal, m/s; ∇ is the nabla operator, m^{-1}; T is the temperature, K; **q** is the vector of specific heat flow due to heat conduction (heat flow density), W/m^2; λ is the coefficient of molecular heat conduction, W/(m·K).

In the mathematical model, heat input from the electron beam and the poured melt is balanced by heat removal from: radiation and evaporation from the mirror of the metal pool; heat transfer from the side surface of the ingot into the mould; radiation from the side surface of the ingot wall to the mould wall below the boundary of separation of their surfaces and the appearance of a gap between them (associated with shrinkage of the metal ingot with a decrease in its temperature); radiation from the ingot surface outside the mould. These factors are taken into account by the boundary conditions [12, 17] listed in Table 1.

Mathematical modeling of hydrodynamic processes during continuous feeding of incompressible titanium melt into the mould was performed using the Navier–Stokes equations for laminar flow. For a stationary process, the model has the form [12, 17, 20, 22]:

$$\rho(\mathbf{u} \cdot \nabla)\mathbf{u} = \nabla \cdot (-p\mathbf{I} + \mathbf{K}) + \mathbf{F}_d + \rho\mathbf{g};$$

$$\mathbf{K} = \mu[\nabla \cdot \mathbf{u} + (\nabla \cdot \mathbf{u})^T]; \; \rho \nabla \cdot \mathbf{u} = 0.$$

Here p is the averaged pressure value, Pa; **I** is the unit tensor; **K** is the viscous stress tensor, Pa; $\mathbf{F}_d$ is the vector of the Darcy braking force, which is artificially introduced to reduce and suppress the velocities in the viscous and solid zones, Pa/m; **g** is the vector of free-fall acceleration, m/s^2; μ is the coefficient of molecular viscosity of the liquid metal, Pa·s.

In the upper equation, in the last term, ρ is a function of temperature T. This involves the idea of he Boussinesq approximation, in which the product ρ**g** affects convection as T changes, since **g** is large enough for this product to be significant.

Darcy braking force, Pa/m, is calculated using the formula from the works [20, 23]:

$$\mathbf{F}_d = \frac{C\left(1 - F_{L-S}\right)^2}{q + F_{L-S}^3}\left(\mathbf{u} - \mathbf{u}_{cast}\right),$$

where $C \approx 10^2$–10^4 kg/(m^{3}s); $q \approx 10^{-2}$–10^{-4} are the values, whose ratio C/q must be sufficient to suppress the flow in a solid metal when $F_{L-S} = 0$ (except for the melting rate of the ingot $\mathbf{u}_{\text{cast}}$). In a liquid metal, when $F_{L-S} = 1$, the Darcy force $\mathbf{F}_d = 0$ and should not affect the flow [23]. In the transition zone, the flow corresponds to the Darcy force. Here F_{L-S} is an approximation function that determines the distribution of the volumes of liquid and solid metal in the two-phase liquidus-solidus zone in the temperature range T_L–T_S.

The hydrodynamic problem uses the boundary conditions [12, 17] from Table 1.

Figure 1 schematically shows a half of the ingot over its conditional cross-section along the vertical axis of symmetry in the middle of the conditional spot on the surface of the pool from the jet of the liquid metal poured into the pool, with the designation of geometric areas G_1–G_7. Therefore, a half of the model is considered, since in this cross-section its conditional parts are symmetrical and identical. The number of nodes in the finite element mesh is $3.1 \cdot 10^6$.

The *boundary* G_1, which is limited by the area of filling melt into the mould, is the entry to the system and can be determined either by an isothermal process with a type 1 condition (first equation), where T_{in} is the metal inlet temperature (temperature of the metal poured from the cold hearth [24]), or by an isobaric process with a type 2 condition for an open wall (second equation [12]), where **n** is the normal vector to the surface; $\mathbf{u}_{\text{in}}$ is the velocity vector of the melt jet at the inlet. Here, p_0 is the initial pressure value at the inlet point of the molten metal flow on the surface of the pool, Pa; **t** is the tangent vector to the surface.

The boundary conditions for the flow velocity in the mould are the absence of penetration through its walls $\mathbf{u} \cdot \mathbf{n} = 0$ and the presence of shear stresses. Therefore, the hydrodynamics problem is solved by assuming the presence of sliding along the boundary. The condition for the liquid metal flow to reach the pool surface, on the contrary, is the presence of penetration into the pool $\mathbf{u} \cdot \mathbf{t} = 0$, but only normal to the surface, with the absence of shear stresses — without sliding along the boundary in side directions.

Table 1. Boundary conditions of the mathematical model [12, 17]

Boundary	Heat flows	Hydrodynamic flows
G_1	$T = T_{in}$ or $-\mathbf{n}\cdot\mathbf{q} = \rho\int_{T_{in}}^{T} C_p dT\cdot\mathbf{u}_{in}\cdot\mathbf{n}$	$\mathbf{n}^T(-p\mathbf{I}+\mathbf{K})\cdot\mathbf{n} = -p_0$; $\mathbf{u}\cdot\mathbf{t} = 0$
G_2	$-\mathbf{n}\cdot\mathbf{q} = q_{eb} - q_{ev} - q_{rad2}$; $q_{eb}=P_{eb}/S_{dz}$; $q_{rad2} = \varepsilon_2\sigma(T_{vault}^4 - T^4)$	
G_3	$-\mathbf{n}\cdot\mathbf{q} = \begin{cases} -q_{conv3}, T_{in}\ge T > T_L; \\ -q_{conv3'} - q_{rad3'}, T_L \ge T \ge T_{sep}; \\ -q_{rad3}, T < T_{sep}; \end{cases}$ $q_{conv3} = h_3(T_{cryst} - T)$; $h_3 = h_L + (h_{in} - h_L)\frac{T - T_L}{T_{in} - T_L}$; $q'_{conv3} = h'_3(T_{cryst} - T)$; $h'_3 = h_L F_{L-sep} + h_{sep}(1 - F_{L-sep})$; $q'_{rad3} = \varepsilon'_3\sigma(T_{cryst}^4 - T^4)$; $\varepsilon'_3 = \varepsilon_3(1 - F_{L-sep})$; $q_{rad3} = \varepsilon_3\sigma(T_{cryst}^4 - T^4)$	$\mathbf{u}\cdot\mathbf{n} = 0$; $\mathbf{K} - (\mathbf{K}\cdot\mathbf{n})\cdot\mathbf{n} = 0$
G_4	$-\mathbf{n}\cdot\mathbf{q} = q_{rad4}$; $q_{rad4} = \varepsilon_4\sigma(T_{wall}^4 - T^4)$	
G_5	$-\mathbf{n}\cdot\mathbf{q} = 0$ or $-\mathbf{n}\cdot\mathbf{q} = \rho\int_{T_{out}}^{T} C_p dT\cdot\mathbf{u}_0\cdot\mathbf{n}$	
G_6		
G_7		$\mathbf{u} = \mathbf{u}_0$

At the *boundary* G_2, which is limited by the area of the molten metal surface in the mould, with the exception of the boundary G_1, there is heating of the melt from the electron beam (type 2 condition), its cooling due to evaporation (type 2 condition) and radiation (type 3 condition) for which: q_{eb} is the specific heat flow from the electron beam heating this surface, W/m^2; P_{eb} is the thermal power from the electron beam, W; S_{dz} is the surface area of the pool of the molten metal, m^2, $S_{dz} = \pi r^2$; r is the radius of the surface of the pool of the molten metal, m. The heat flow q_{eb} is distributed across the surface of the molten metal pool either uniformly or (and) according to a Gaussian distribution along the radius. In the latter case, the Gaussian distribution of the heat power from the electron beam on the surface of the pool and the radius of the spot from the beam are taken into account; q_{ev} is the specific heat flow caused by the evaporation of the liquid metal from the surface of the pool, W/m^2; q_{rad2} is the specific heat flow of radiation from the surface of the liquid metal pool, W/m^2 [25]; ε_2 is the dimensionless emissivity coefficient of the system of surfaces of the following bodies: liquid metal of the pool surface — vault of the vacuum chamber, between which the process of radiant heat exchange takes place; $\sigma = 5.67\cdot10^{-8}$ W/(m$^2\cdot$K^4) — Stefan–Boltzmann constant; T_{vault} is the temperature of the vacuum chamber vault above the pool surface. The emissivity coefficient for the system of surfaces of two bodies a and b at the i-th boundary is calculated using the formula [26]:

$$\varepsilon_i = (\varepsilon_a^{-1} + \varepsilon_b^{-1} - 1)^{-1};$$

ε_a and ε_b are the emissivity coefficients for the corresponding surfaces.

At the *boundary* G_3, which is limited by the walls of the mould, both conductive and radiant heat transfer occur (type 3 conditions), where: q_{conv3} is the specific heat flow in the case of conductive heat exchange, W/m^2, passing over the height of the mould wall area with a temperature T_{cryst}, which is in contact with the liquid metal having a temperature above the liquidus temperature T_L [25]; h_3 is the heat transfer coefficient from the surface of the liquid metal of the ingot, which integrally takes into account the heat transfer from it through the mould wall to the cooling water, W/(m$^2\cdot$K). In this area, it is assumed that with a decrease in the melt temperature, it linearly decreases

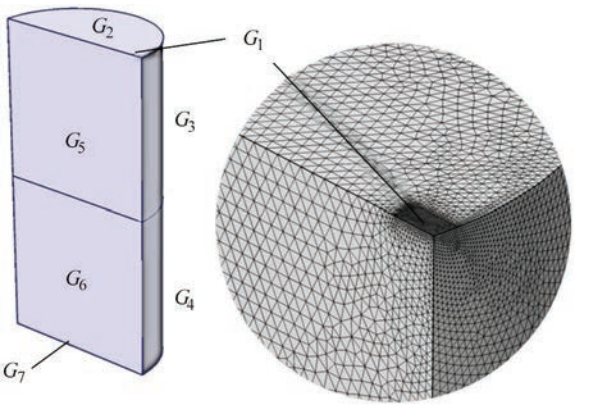

Figure 1. Geometric model and a fragment of the finite element mesh in the region of metal pouring

from the value h_{in} to the value h_L; q'_{conv3} is the specific heat flow in the case of conductive heat exchange, W/m^2, passing along the height of the mould wall area that is in contact with the metal ingot, which has a temperature lower than the liquidus temperature T_L and higher than the temperature at which the ingot is separated from the mould wall T_{sep} due to the shrinkage of the metal as a result of its cooling; h'_3 is the heat transfer coefficient from the surface of the metal ingot, which integrally takes into account the heat transfer from it through the mould wall to the cooling water, W/(m^2·K). In this area, it is assumed that with a decrease in the metal temperature, h'_3 decreases according to the approximation function $F_{L–\text{sep}}$ (by analogy with the function $F_{L–S}$) from the value h_L to the value h_{sep}; q'_{rad3} is the specific heat flow caused by radiation from the metal ingot surface, W/m^2, which falls on the area of the mould wall with the temperature of the metal ingot below the liquidus temperature T_L and above the temperature of the ingot separation from the mould wall T_{sep}; ε'_3 is a dimensionless coefficient of the reduced emissivity for the system of surfaces of bodies in this area; ε_3 is a dimensionless coefficient of the reduced emissivity for the system of surfaces of bodies of the metal ingot and the mould wall, between which the process of radiant heat exchange occurs; q_{rad3} is a specific heat flow caused by radiation from the surface of the metal ingot, W/m^2, falling on the area of the mould wall with a metal ingot temperature below the temperature of the ingot separation from the mould wall T_{sep}.

At the *boundary* G_4, which is limited by the vertical walls of the ingot yielded from the mould, only radiant heat exchange occurs (type 3 condition), where q_{rad4} is the specific heat flow of radiation from the side surface of the metal ingot, W/m^2, falling on the wall of the vacuum chamber with a temperature T_{wall}, ε_4 is a dimensionless emissivity coefficient for the system of surfaces of bodies metal ingot and wall of the vacuum chamber in this area.

At the *boundaries* G_5 *and* G_6, which are limited by the cross-sectional plane passing along the vertical axis of symmetry of the ingot along its height, type 2 condition is observed.

The *boundary* G_7 is limited by the cross-sectional plane of the of the lower part of the ingot at such a distance from its upper part where thermal processes no longer affect the thermal processes in its upper part in the region of the metal crystallization front. This boundary is a conditional exit from the system. The distance to it is determined by iterative calculation. At this boundary, one can choose either type 2 condition of an adiabatic process of a closed wall (thermal insulation) (first equation), or type 2 condition of isobaric process for an open wall (second equation [12]), where T_{out} is the approximate value of the temperature at the boundary G_7, which is specified during the calculations; $\mathbf{u}_0$ is the vector of ingot withdrawal rate, m/s.

The vault and walls of the vacuum chamber are water-cooled.

To calculate thermal and hydrodynamic processes with a present phase transition in metal, a finite element numerical method with a fixed calculation mesh was used, in which the liquid and solid phases are considered as a single region. The interphase region is located between temperatures T_L and T_S and is considered as a viscous transition zone, the parameters of which change relative to the volume fractions of the phases according to a certain law. The liquid phase is present at temperatures above the liquidus temperature T_L, and the solid phase is present at temperatures below the solidus temperature T_S.

The volume fraction of $F_{L–S}$ liquid in the two-phase zone as a function of temperature is described by a smoothed function using the erf error function, which is an internal function of many computer calculation software packages:

$$F_{L–S}(T) = \begin{cases} 0, T < T_S; \\ \dfrac{y_{\max} - y_{\min}}{2} \times \\ 1, T_L < T, \end{cases}$$

$$\times \left[1 + \operatorname{erf} \left(\frac{x - \dfrac{x_{\min} + x_{\max}}{2}}{\dfrac{x_{\max} - x_{\min}}{x_{\max,\text{erf}} - x_{\min,\text{erf}}}} \right) \right] +$$

$$+ y_{\min}, T_S \le T \le T_L;$$

where $y_{\min} = 0, y_{\max} = 1$; $x_{\min}, x_{\max}$ are the specified minimum and maximum values on the abscissa axis, at which the minimum and maximum values of the $F_{L–S}$ function approach 0 and 1 (here $x_{\min} = T_S$, $x_{\max} = T_L$); $x_{\min,erf}$, $x_{\max,erf}$ are the minimum and maximum values on the abscissa axis of the erf function itself, at which it approaches the values on the ordinate axis –1 and 1. Usually, if $x_{\min,erf} = –2$, the function $erf(–2) = –0.99532$, and if $x_{\max,erf} = 2$, the function $erf(2) = 0.99532$, which is a sufficient approximation to –1 and 1. But if a greater approximation is necessary, we can take the value $x_{\min,erf} = –e$, where the function $erf(–e) = –0.99988$, and if $x_{\max,erf} = e$, the function $erf(e) = 0.99988$.

In the two-phase liquidus-solidus transition zone, the $F_{L–S}$ curve has a growing dependence, and for $(1 – F_{L–S})$ — a falling dependence (Figure 2). By analogy with the $F_{L–S}$ function, the $F_{\alpha–\beta}$ function was also applied in the corresponding temperature range of the α–β phase transition.

For the alloy under consideration, the following temperatures are specified: at the artificially expanded boundaries of the α-β phase transition, $T_\alpha = 1253$ K, $T_\beta = 1283$ K for the actual temperature $T_{\alpha–\beta} = 1283$ K

[27]; at the boundaries of the *S–L* phase transition, T_S = 1873 K, T_L = 1923 K, with an actual temperature $T_{L–S}$ = 1923 K [27]; the temperature at which the ingot is separated from the mould wall T_{sep} = 1640 K; the temperature of the metal at the mould inlet T_{in} = 2061 K. Latent heat of phase transitions (change in system enthalpy) [27]: $H_\alpha - H_{25} = 6.36 \cdot 10^5$ J/kg, $H_\beta - H_{25} = 6.84 \cdot 10^5$ J/kg and $H_{\alpha–\beta} = H_\beta - H_\alpha = 4.8 \cdot 10^4$ J/kg; $H_S - H_{25} = 1.180 \cdot 10^6$ J/kg, $H_L - H_{25} = 1.466 \cdot 10^5$ J/kg and $H_{L–S} = H_L - H_S = 2.86 \cdot 10^5$ J/kg; H_{25} is the initial enthalpy of the system at 25 °C (298 K).

THERMOPHYSICAL PARAMETERS

take into account their changes from temperature and α–β and *L–S* phase transitions, while the specific heat capacity of metal also takes into account the latent heat of phase transitions, which were calculated using the methodology described in [18].

The finite element numerical method is sensitive to discontinuities and step jumps in function values, when the method cannot always find a solution and calculations fail. Step changes in the thermophysical characteristics of titanium alloys are present at α–β and *L–S* phase transitions. It is necessary to make such a mathematical description of the functions in order to achieve a smooth transition of values in the zone of step jumps. For this purpose, an approach known in modelling of thermal processes was used, involving a slight artificial expansion of the ranges of such zones [13] in which the values of characteristics change smoothly. In the case under consideration, this is conveniently implemented by the functions $F_{\alpha–\beta}$, $1 - F_{\alpha–\beta}$, $F_{L–S}$ and $1 - F_{L–S}$, taking into account the increase or decrease in values in phase transitions. The approximations of the thermophysical parameters are performed namely in this way (Figure 3) [12].

Figure 3 shows the approximation curves of the simulated thermophysical characteristics of Ti–6Al–4V titanium alloy as a function of temperature, obtained from the data in [27]. Similar dependencies for Ti–6Al–7Nb alloy have not been found in the literature. However, the characteristics of these related alloys are very similar, so the ratios for the first alloy can be applied to the second alloy with a sufficiently close approximation. Moreover, the specific heat capacity C_p for Ti–6Al–7Nb alloy can be specified using existing methods.

For an approximate calculation of the heat capacity of titanium alloys, the Neuman–Kopp rule (the rule of additive heat capacity) can be used. This is an empirical method for estimating the specific heat capacity of multicomponent alloys and complex materials based on the heat capacities of their constituent elements. The approach is based on the assumption that the total specific heat capacity of the alloy is the sum of the heat capacities of its individual components. For an

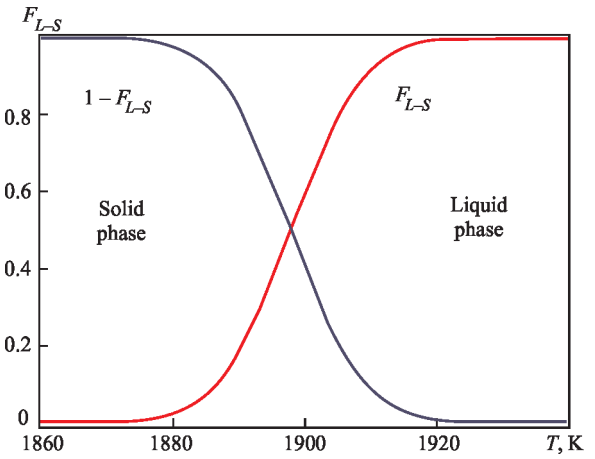

Figure 2. Dependence of the volume fraction of liquid on temperature in the two-phase zone when using the $F_{L–S}$ and $(1 - F_{L–S})$ functions

approximate estimate of the specific heat capacity of the alloy C_p, the following ratio is used:

$$C_p = \sum_{i=1}^{n} N_i C_{p,i},$$

where N_i is the mass fractions of the i-th component of the alloy, %; $C_{p,i}$ is the specific heat capacity of the *i*-th component of the alloy; *n* is the number of components of the alloy.

Based on this approach, the heat capacity values for Ti–6Al–4V and Ti–6Al–7Nb alloys were calculated. The C_p values obtained using the Neumann–Kopp rule for Ti–6Al–7Nb alloy are lower than the C_p values for Ti–6Al–4V alloy obtained using the same rule by an average of 3 % over the entire calculated temperature range of 300–2800 K. However, if we compare the calculated values of heat capacity C_p obtained using the Neumann–Kopp rule and the existing data for Ti–6Al–4V alloy [27], the discrepancy between them in the temperature range from 300 to 1800 K does not exceed 5 %, and from 1800 K to 2800 K it increases to 17 %, which indicates the insufficient accuracy of this approach at high temperatures.

The second, more accurate approach to calculating the specific heat capacity of Ti–6Al–7Nb alloy is based on the already known values of the dependence of C_p on the temperature of Ti–6Al–4V alloy [27]. Since Ti–6Al–4V and Ti–6Al–7Nb alloys differ only in V and Nb elements, and to a small extent, in the Ti content, it is worth applying the approach of additive contribution of elements to the heat capacity.

This approach is based on the use of the rule of total contributions, according to which the specific heat capacity of a multicomponent alloy can be expressed as a linear combination of the heat capacities of its constituent elements, which can be described as follows:

$$C_p(T)_{\text{Ti–6Al–7Nb}} = C_p(T)_{\text{Ti–6Al–4V}} + \Delta C_p.$$

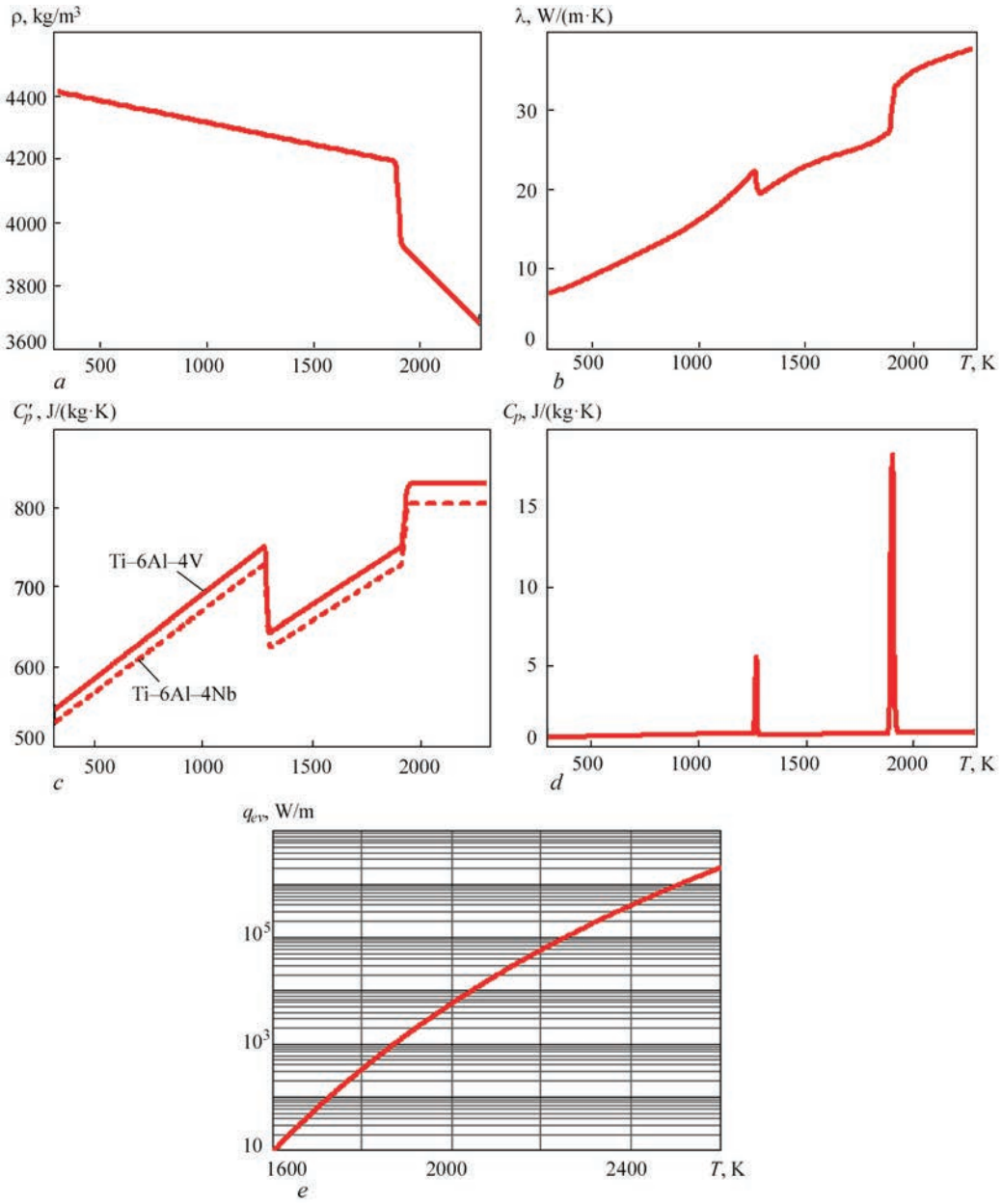

Figure 3. Approximation dependencies of the modelled thermophysical parameters of Ti–6A1–7Nb titanium alloy on temperature T: *a* — density ρ; *b* — thermal conductivity λ; *c* — specific heat capacity C'_p, *d* — specific heat capacity C_p taking into account the latent heat of α–β and *L*–*S* phase transitions; *e* — evaporation losses q_{ev} from the surface of the Ti melt

Here, ΔC_p is a correction that takes into account the difference in the heat capacities of V and Nb. The heat capacity of pure V and Nb is available from literature sources and can be used to calculate the contribution of substituted atoms:

$$\Delta C_p = (C_{p,\mathrm{Nb}} - C_{p,\mathrm{V}}) \cdot \Delta\omega,$$

where Δω is the difference in the content of substituted elements.

As a result, the calculated heat capacity values for Ti–6A1–7Nb alloy were found to be lower than the known data for Ti–6A1–4V alloy by an average of 3 % over the entire temperature range of 300–2800 K. This indicates the high accuracy of the used approach. Figure 3 shows the known dependence of $C_p(T)$ for Ti–6A1–4V alloy [27] and the calculated dependence for Ti–6A1–7Nb alloy, which was used for the calculations.

Regarding losses to evaporation from the melt surface (Figure 3, *d*). No such data has been found in the literature for Ti–6A1–4V and Ti–6A1–7Nb alloys. Therefore, it is necessary to use known data for pure titanium. This is acceptable since the alloying elements for these alloys constitute 10 and 13 % of the specific masses of the alloys, respectively.

In [28], an approximate formula is given that describes the dependence of the logarithm of the pressure P of saturated titanium vapour on temperature T, K:

$$\lg P(T) = -A \cdot T^{-1} + B - C \cdot \lg(T),$$

where the approximation coefficients for Ti are: $A = 22964$; $B = 10.581$ and $C = 0.373$.

The saturated vapour pressure is equal to $P(T) = 10^{\lg P(T)}$.

Using the Langmuir equation [30], the evaporation rate of titanium, kg/(m²·s), is determined

$$J_{ev}(T) = P(T)\sqrt{\frac{M_{mol}}{2 \cdot \pi \cdot R \cdot T}}.$$

Here, M_{mol} is the atomic (molar) mass of Ti, M_{mol} = = 0.047867 kg/mol; R is the universal gas constant, R = 8.31446261815324 J/(mol·K).

From the known value of the latent molar heat of evaporation of titanium $\Delta H_{ev,mol}$ = 410 kJ/mol [28], its latent heat of evaporation is calculated:

$$\Delta H_{ev} = \Delta H_{ev,mol}/M_{mol} = 8565.4 \text{ kJ/kg}.$$

The specific power of titanium evaporation losses depending on temperature is equal to

$$q_{ev}(T) = J_{ev}(T)\,\Delta H_{ev}$$

and is shown in Figure 3, *d*.

RESULTS AND ANALYSIS OF MATHEMATICAL MODELLING OF LAMINAR HYDRODYNAMIC PROCESSES AND TEMPERATURE FIELDS IN THE INGOT

Three-dimensional mathematical modelling was performed for a system of laminar hydrodynamic processes and temperature fields in the ingot in a continuous mould with an internal diameter of 110 mm and a height of 150 mm at a mass withdrawal rate of the ingot (melting rate) of 20 kg/h. The pouring of preliminary molten metal from a cold hearth onto the surface of the pool occurs near the mould wall into a conditionally square spot of 10×10 mm (equivalent diameter is 11.3 mm). The rate of metal pouring into the pool and its pressure on its surface are taken into account by the boundary conditions at the boundary G_1 (Table 1). The surface of the liquid metal pool is heated by a 16 kW power electron beam with an efficiency of 75 %, which moves in a circle around the periphery of the pool according to the Gaussian distribution of the electron beam thermal power (Figure 4).

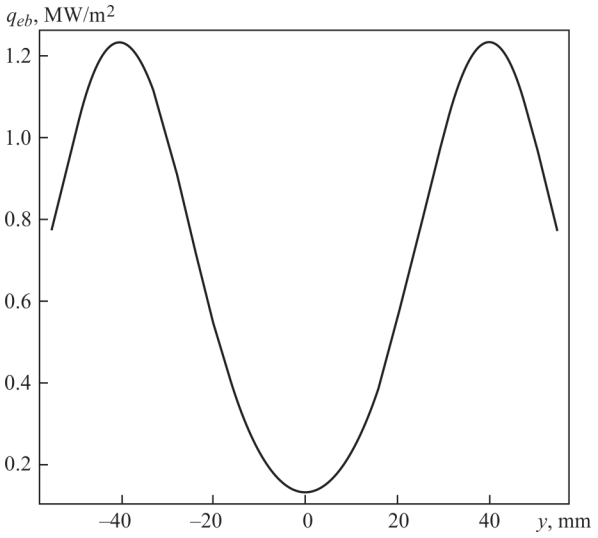

Figure 4. Distribution of the thermal power of the electron beam q_{eb} over the ingot surface (along the y coordinate)

Based on the developed mathematical model, temperature fields and hydrodynamic flows were calculated for the case of forming a Ti–6Al–7Nb titanium alloy ingot using the EBM method. Here, the temperature-dependent thermophysical characteristics of the metal were used, and interphase transition zones were taken into account. This allowed identifying the regularities of the distribution of hydrodynamic flows in the liquid metal and temperature fields, as well as the metal crystallization front during ingot formation.

Figure 5, *a* shows the directions of the velocity vectors of the liquid metal flows, excluding the withdrawal rate of the ingot towards the bottom in the axial direction. A cross-section along the vertical axis of symmetry of the ingot is considered in the middle of the conditional spot on the surface of the pool from the jet of the liquid metal poured into the pool. The size of the vectors is selected on a logarithmic scale proportional to the velocity of the melt.

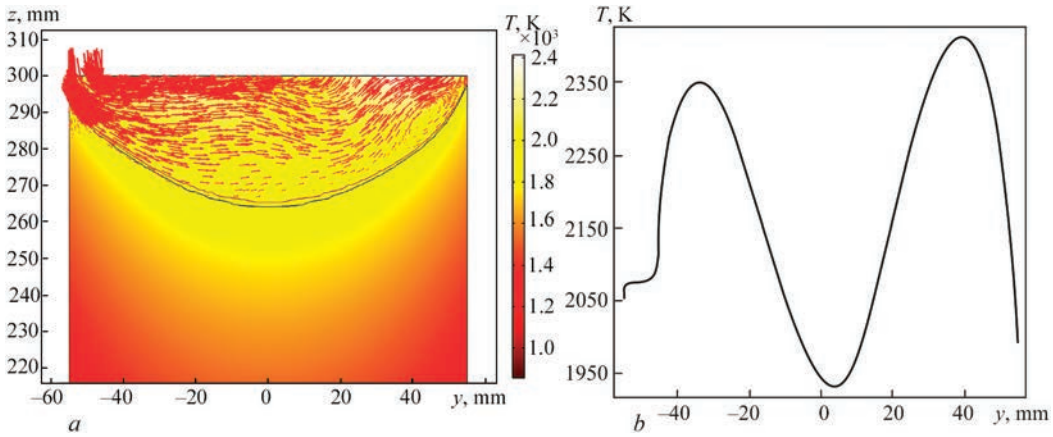

Figure 5. In the section (along the *y* coordinate) along the vertical axis of symmetry of the ingot (*z* coordinate) at the centre of the conditional spot on the surface of the pool from the jet of liquid metal poured into the pool, the following are presented: *a* — flows of the liquid metal in the pool; *b* — temperature on the surface of the pool

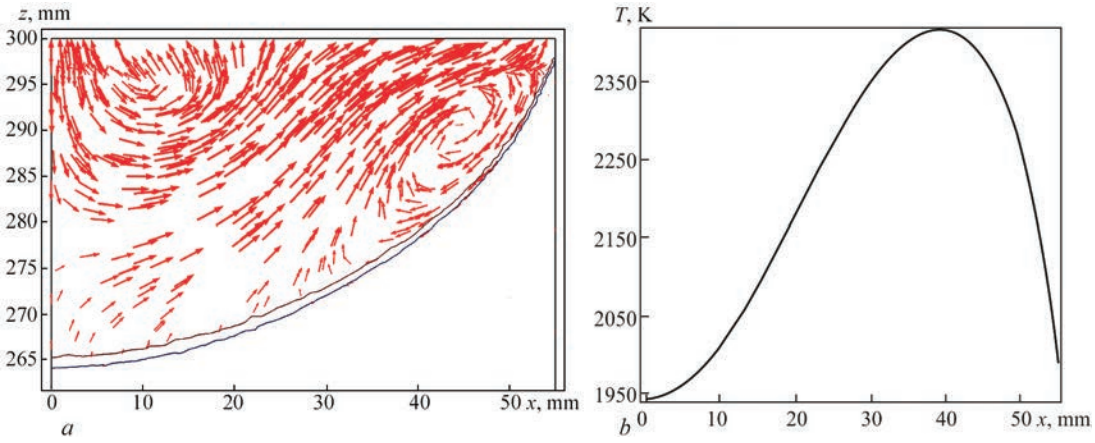

Figure 6. In the section at an angle of 90° (along the x coordinate) along the vertical axis of symmetry of the ingot (z coordinate), the following are presented: *a* — flows of the liquid metal in the pool; *b* — temperature on the surface of the pool

Figure 5, *b* shows a diagram of the temperature distribution on the pool surface of the liquid metal according to the Gaussian distribution of the thermal power of the electron beam around the periphery of the melt.

Figure 6, *a* shows the directions of the velocity vectors of the liquid metal flows, excluding the withdrawal rate of the ingot towards the bottom in the axial direction. A cross-section along the vertical axis of symmetry of the ingot at an angle of 90° from the centre of the conditional spot on the surface of the pool from the jet of the liquid metal poured into the pool is considered. This plane is perpendicular to the plane shown in Figure 5, *a*. Only half of the figure is shown, since the other half is symmetrical.

Figure 6, *b* shows a diagram of the temperature distribution on the surface of the molten metal pool.

Figure 7 shows the three-dimensional distribution of the temperature field and the directions of the velocity vectors of the metal flow in the mould, excluding the withdrawal rate of the ingot towards the bottom.

Flows of the liquid metal (Figure 5, *a*) spread from the point of its pouring on one side of the mould wall to the opposite side of the wall, forming a small vortex near the latter. The figure shows the isotherms of the liquidus T_L (upper curve) and solidus T_S (lower curve) at the boundary of the crystallization front. The position and geometry of this front (Figure 5, *a*, Figure 6, *a* and Figure 7) largely determine the quality of the ingot formation and the concentration of alloying elements in its volume. The flatter the front, the more homogeneous the structure of the solid metal ingot in the radial direction.

An important criterion for the quality of titanium alloy ingots is the smooth appearance of their side surfaces. Therefore, during melting, it is necessary to

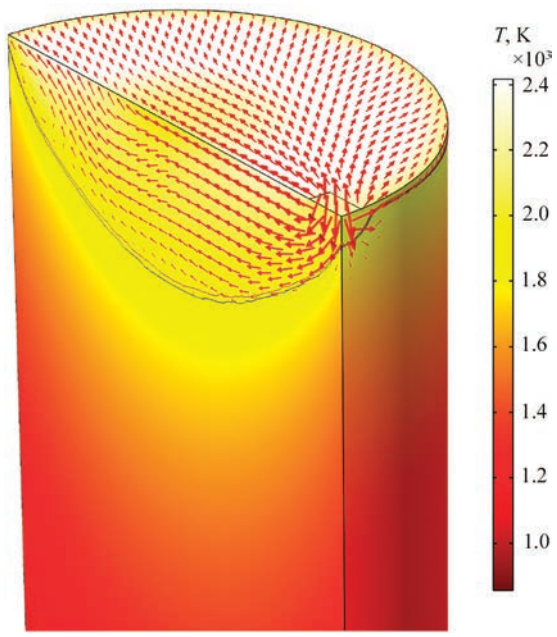

Figure 7. Three-dimensional distribution of the temperature field and metal flows in the mould, excluding the rate of ingot withdrawal to the bottom

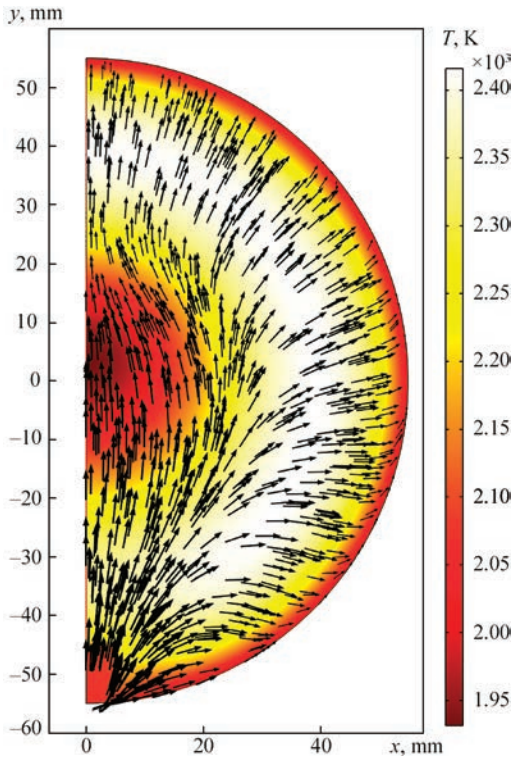

Figure 8. Distribution of the temperature field and metal flows in the mould (top view along the x and y coordinates)

minimize the contact of the liquid metal pool with the mould wall in order to avoid corrugations on the side surfaces of the ingots.

The correct choice of the electron beam position in the radial direction on the pool surface ensures the condition that the liquid metal in the pool has less contact with the mould wall, and the intensity of the beam provides the desired depth and geometry of the crystallization front. The diagram of the temperature distribution on the surface of the molten metal pool (Figure 5, *b*) shows that the maxima on the curve are predetermined by the concentrations of thermal power introduced by the electron gun beam. This temperature distribution ensures the required shape of the metal crystallization front in Figure 5, *a*.

In the cross-section of the ingot in Figure 5, *a*, a single vortex flow is observed.

Figure 8 shows the distribution of the temperature field and metal flows in the mould (top view), and Figure 9 shows the three-dimensional distribution of the molten metal flows in the ingot.

The flows of the molten metal for different vertical cross-sections of the ingot in Figures 5, *a* and 6, *a* are different, as they depend on the place where the liquid metal is poured into the mould. This is seen in the three-dimensional distribution of the temperature field and metal flows in the mould (Figures 7 and 8) and the melt flows in the ingot (Figure 9). In the top view (Figure 8), a pronounced diametrical distribution of metal flows is observed, which is caused by the action of flows from the liquid metal poured into the mould and the thermal power from the electron beam.

Analysis of the results obtained using the mathematical model showed that the velocity of the liquid metal in the mould at the point of pouring is $18 \cdot 10^{-3}$ m/s, and the velocity of a circumferential flow closer to the centre of the mould on the pool surface is ~$2 \cdot 10^{-3}$ m/s (Figure 9), which corresponds to Reynolds numbers Re ≈ 260 and 125, the value of which characterises the laminar flow of the melt in the pool.

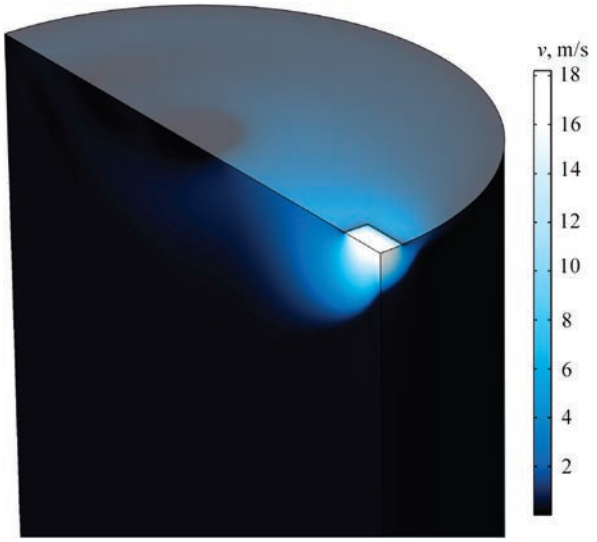

Figure 9. Three-dimensional distribution of the molten metal flows in the ingot with the scale of their velocity *v*

Figure 10 shows the directions of the liquid metal flows, taking into account the rate of ingot withdrawal downwards in the axial direction. A cross-section along its vertical axis of symmetry is considered in the middle of the conditional spot on the pool surface from the jet of the liquid metal poured into the pool.

The results of calculations of metal trajectories confirmed the adequate use of the Darcy function to suppress the metal movement in the solid phase.

ANALYSIS OF THE RESULTS OF MATHEMATICAL MODELLING OF THE INFLUENCE OF EBM TECHNOLOGICAL PARAMETERS ON LAMINAR HYDRODYNAMIC PROCESSES AND TEMPERATURE FIELDS IN THE INGOT

Mathematical modelling was performed for different positions of the electron beam centre relative to the vertical axis of symmetry of the ingot and different withdrawal rates.

In order to determine how the position of the electron beam, moving in the azimuthal direction along the surface of the ingot, affects the melt pool, Figure 11 shows the temperature distribution on the surface of the pool for different positions of the electron beam centre relative to the vertical axis of symmetry of the ingot at distances of 39, 41, 43 (operating mode), 45 and 47 mm. Figure 12 shows the temperature distribution and crystallization profiles of the metal and two-phase zones in the case of the electron beam position relative to the vertical axis of symmetry of the ingot: *a* — at a distance of 39; *b* — 43 (operating mode); *c* — 45 mm. It is seen that the position of the beam significantly affects the geometry of the pool. The closer the beam rotates to the centre (39 mm), the higher the temperature on the surface of the melt (Figure 11) and the deeper the pool becomes (Figure 12, *a*). When the beam is moved away from the centre of the mould (43 mm — operating mode), the

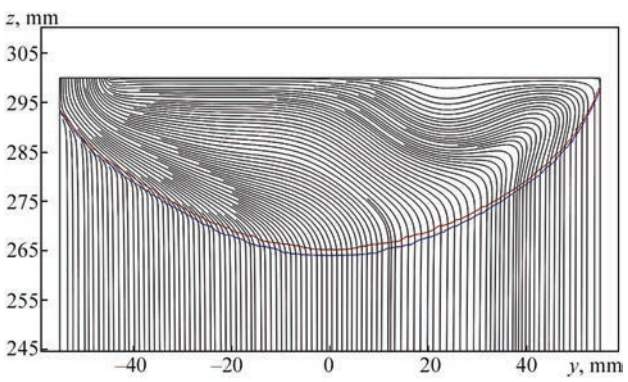

Figure 10. Directions of flows of the liquid metal taking into account the rate of ingot withdrawal to the bottom in the axial direction (along the *z* coordinate) in the cross-section (along the *y* coordinate) along its vertical axis of symmetry

temperature on the surface of the melt decreases and reaches the liquidus temperature T_L of the melt in the lower part of the curve (Figure 11), which is optimal, and the pool decreases in depth (Figure 12, *b*). In this case, the crystallization profile becomes flatter, which is the desired result. When the centre of the beam is moved by 45 mm from the vertical axis of symmetry of the mould, the temperature at the bottom of the curve becomes lower than the solidus temperature T_S (Figure 11) and an island of solidified metal appears on the surface of the pool (Figure 12, *c*), while the pool decreases in depth. However, this is an unacceptable mode due to the appearance of unmelted metal on the surface of the pool. If the centre of the beam is moved by 47 mm, the temperature on the surface of the pool becomes even lower (Figure 11), and the proportion of unmelted metal increases.

A significant cause for the decrease in temperature on the surface of the melt when the centre of the electron beam is moved from the vertical axis of symmetry of the mould towards its wall is that a significant part of the beam hits the upper end of the mould wall rather than the surface of the melt. This reduces the useful power for heating the melt.

Figure 13 shows how the temperature field distribution, flows of the liquid metal, its crystallization profiles and two-phase zones change at different rates of melt pouring into the mould and, accordingly, at different withdrawal rates of the ingot. It is seen that as the rate of pouring the melt increases, the depth of the pool increases significantly, and its profile becomes more concave.

A flatter metal crystallization front of the metal ingot, which is desired, is formed at lower rates of melt pouring into the mould and, accordingly, at lower rates of ingot withdrawal.

Figure 14, *a* and b shows the interpolation dependencies of the liquid metal pool depth *l* and the liquid metal pool shape coefficient k_f, which is equal to the ratio between the mould diameter d_{kr} and the pool depth *l*, $k_f = d_{kr}/l$, on the mass withdrawal rate of the ingot v_g, which pass through six calculation points corresponding to the pool depths in Figure 13.

With an increase in the mass withdrawal rate of the ingot above 10 kg/h, the pool depth grows linearly, and the coefficient k_f decreases.

In the case of a mass melting rate of 20 kg/h and an electron beam heating power of 16 kW in the mould, a crystallization front close to flat one is formed, and

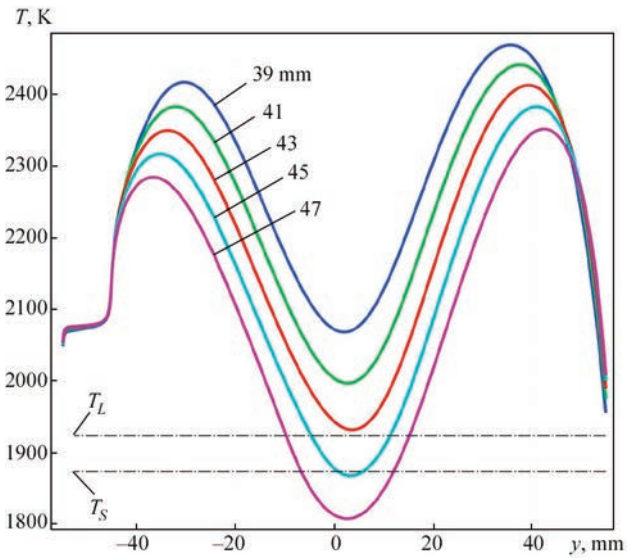

Figure 11. Temperature on the surface of the melt pool in the case of different position of the electron beam centre relative to the vertical axis of symmetry of the ingot (along the *z* coordinate) at distances (along the *y* coordinate) of 39, 41, 43 (operating mode), 45 and 47 mm

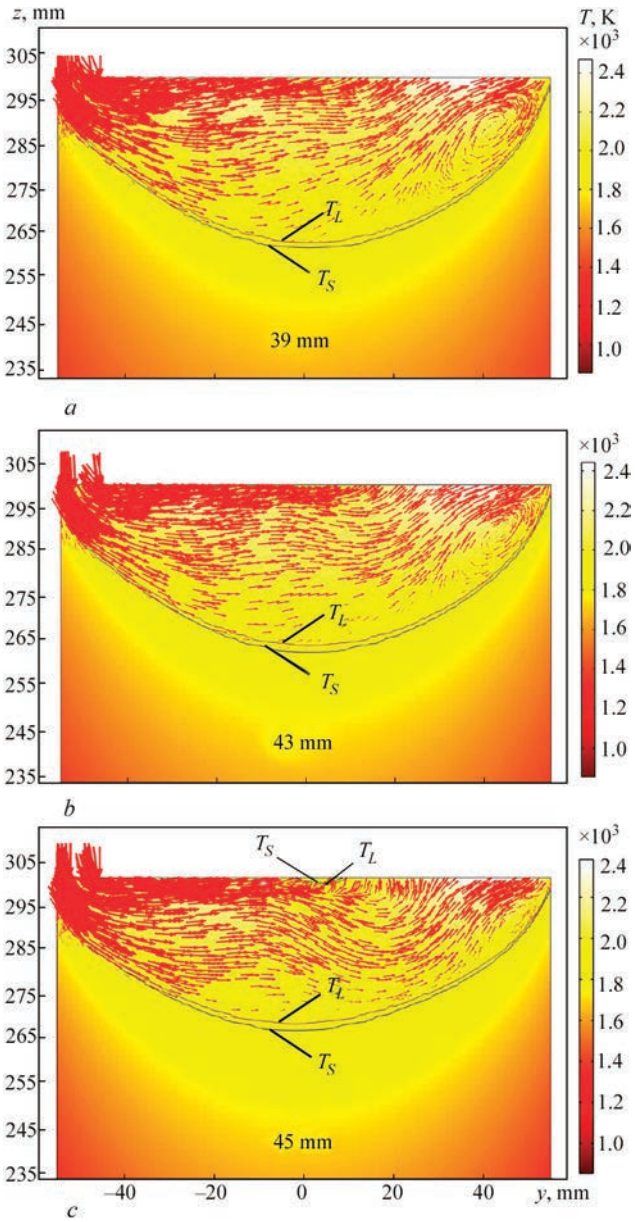

Figure 12. Temperature distribution and profiles of metal crystallization and two-phase zones (along the *y* coordinate) in the case of different position of the electron beam relative to the vertical axis of symmetry of the ingot along the *z* coordinate: *a* — at a distance of 39; *b* — 43 (operating mode); *c* — 45 mm

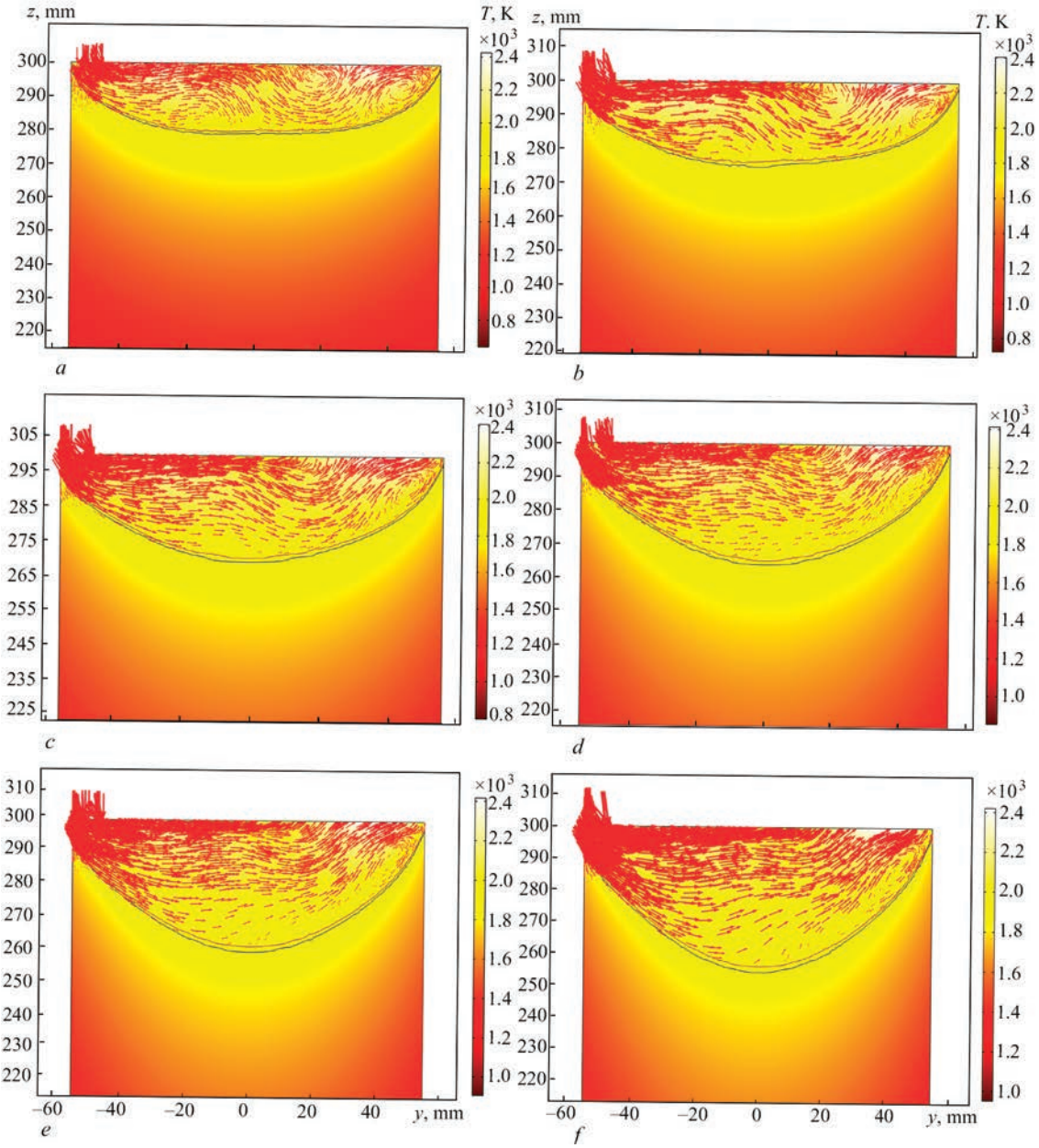

Figure 13. Distribution of the temperature field, flows of the liquid metal and profiles of its crystallization and two-phase zones (along the *y* and *z* coordinates) in the case of different mass rates of ingot withdrawal (along the z coordinate), kg/h: *a* — 5; *b* — 10; *c* — 15; *d* — 20 (operating mode); *e* — 25; *f* — 30

the pool shape coefficient is 3.24, i.e. the depth of the melt pool is 3.24 times less than its width.

Figure 15 shows the temperature distribution on the surface of the melt pool for different mass withdrawal rates of the ingot: 5, 10, 15, 20 (operating mode), 25 and 30 kg/h. For rates of ingot withdrawal of 10–30 kg/h, the position of the electron beam centre relative to the vertical axis of symmetry of the ingot was at a constant distance of 43 mm, which corresponds to the operating mode. For a mass rate of 5 kg/h, this distance was taken smaller — 41 mm in order to ensure a complete melting of the metal on the pool surface, since at a distance of 43 mm in this mode, an island with solidified metal is formed in the center of the pool surface, which is unacceptable. Reducing this distance to 41 mm led to an increase in the temperature on the pool surface, and accordingly to a rise in the temperature distribution curve (Figure 15) for a mass rate of 5 kg/h. This caused the appearance of a nonlinear region on the diagrams (Figure 14, *a*) for a mass rate of less than 10 kg/h.

In order to assess the adequacy of the plotted mathematical model, an ingot with a diameter of 110 mm was metled from an experimental complex-alloy titanium alloy, close in physical properties to Ti–6A1–7Nb alloy, in which the metal crystallization profiles are clearly displayed. A longitudinal template was cut out from the upper part of this ingot and its macrostructure was revealed by etching. A great number of alloying elements in the experimental alloy allowed a clear identification of the crystallization profiles at different melting rates. Figure 16 shows

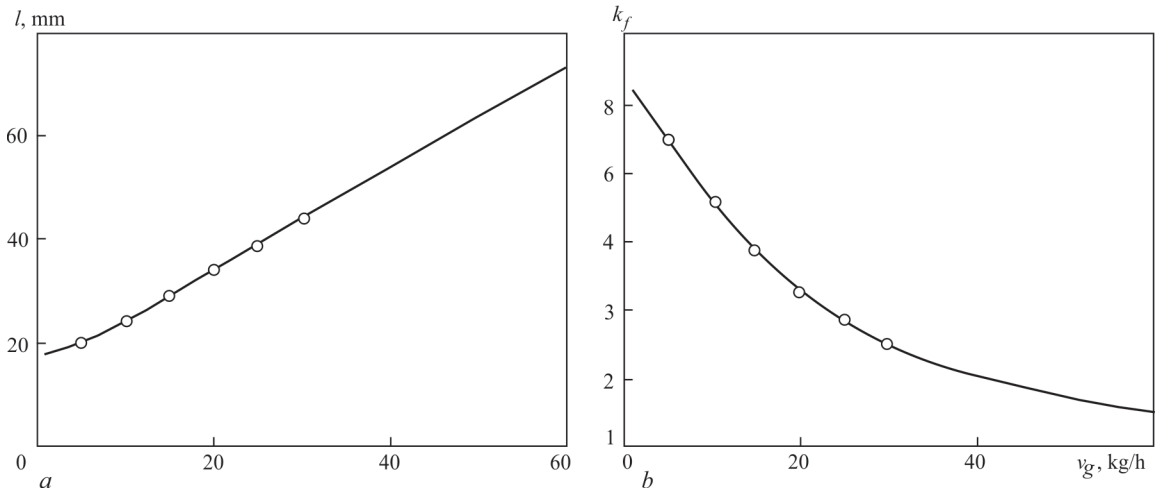

Figure 14. Interpolation dependences on the mass rate of ingot withdrawal v_g: *a* — depth of the liquid metal pool l; *b* — shape coefficient of the liquid metal pool k_f

a macrosection of the template of the upper part of the ingot, cut out in the axial plane and with marked contours of the ingot crystallization fronts on it: solid lines are real contours; dashed lines are calculated contours. In this Figure, the lower crystallization profile, marked with a light solid line, corresponds to the operating mass rate of ingot withdrawal of 20 kg/h.

At the final stage of ingot melting, the melting rate decreases. In Figure 16, two more crystallization profiles are marked with light solid lines, which correspond to the mass withdrawal rate of the ingot at the level of 15 and 10 kg/h. This Figure also shows the calculated light dashed lines of the crystallization profiles for mass rates of 10 kg/h from Figure 13, *b*; 15 from Figure 13, *c* and 20 from Figure 13, *d*. Comparison of the real contours of the ingot crystallization fronts, indicated by solid lines, and the calculated contours of the crystallization fronts, plotted on the figure by light dashed lines, indicates a good coincidence of the front profiles and acceptable accuracy of the results of mathematical modeling for the laminar nature of the melt flow movement.

The macrosection of the lower working area of the ingot (Figure 16) is characterized by the absence of cavities and discontinuities, and the macrostructure of the ingot has crystals close to equiaxed, which is an indice of a high ingot quality. The upper part of the ingot, formed at the final stage of melting and removal of the shrinkage cavity, is characterized by large non-equilibrium crystals, has a different composition of alloying elements due to their evaporation and is not considered to be one that provides an acceptable metal quality. Therefore, it is cut off and remelted during subsequent ingot melting.

Thus, for EBM of titanium alloys in a mould with a diameter of 110 mm, as a result of comparing the calculated profile of the crystallization front of the metal

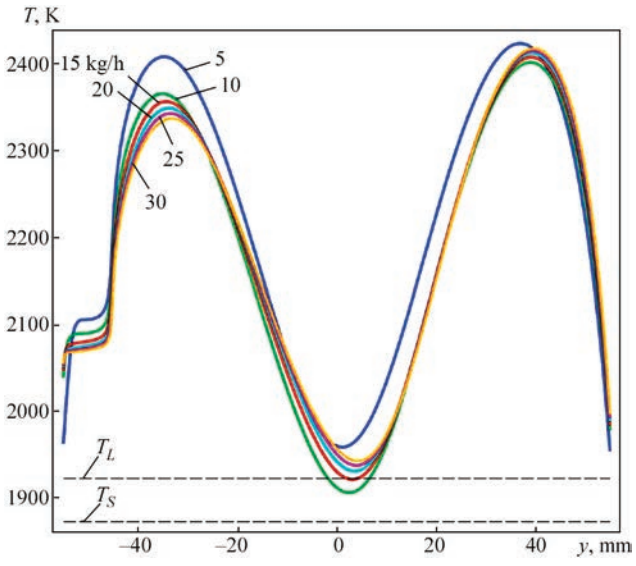

Figure 15. Temperature distribution on the surface of the melt pool (along the y coordinate) in the case of different mass rates of ingot withdrawal, kg/h: 5, 10, 15, 20 (operating mode), 25 and 30

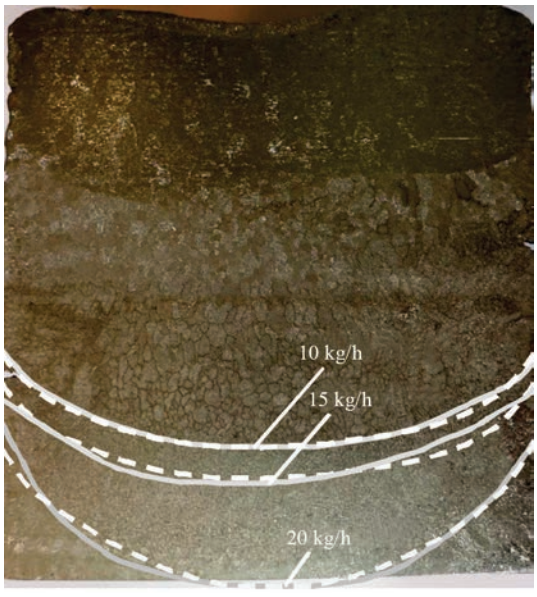

Figure 16. Macrosection of the template of the upper part of the ingot, cut out in the axial plane and with the contours of the ingot crystallization fronts marked on it: solid lines are real contours; dashed lines are calculated contours

in the ingot with the actual crystallization profile of the molten ingot, it was established that the laminar representation of hydrodynamic flows of the liquid metal in the ingot gives a result closer to the real profile than their turbulent representation from [12].

Analysis of the obtained results showed that heat transfer in the liquid phase of the ingot in the laminar mode is mainly predetermined by heat and mass transfer due to the movement of the molten metal, and the power of the electron beam and the type of its coverage of the surface of the pool have a very significant effect on the depth and shape coefficient of the melt pool in the mould.

According to the calculated modes, high-quality ingots with a diameter of 110 mm of medical titanium Ti–6A1–7Nb alloy alloy with a practically homogeneous metal structure were melted at the PWI [30].

Factors that affected the accuracy of the calculations include the simplifications and assumptions used in the development of the mathematical model, which did not significantly affect the overall trends in ingot formation during EBM. Further research should focus on improving the mathematical model with fewer simplifications and assumptions.

Mathematical modeling has made it possible to eliminate the very costly method of sampling to determine technological modes from the preparation for conducting a technological process and is useful and relevant for foundry engineers.

CONCLUSIONS

1. A three-dimensional mathematical model of thermal and stationary laminar hydrodynamic processes based on the Navier–Stokes equations in the melt of a cylindrical ingot has been developed. The ingot is melted by the method of electron beam melting, in which the beam moves along the circumference of the melt pool periphery according to the Gaussian distribution of thermal power from the beam.

2. According to the results of mathematical modeling, the temperature fields and laminar hydrodynamic flows of the molten metal in Ti–6Al–7Nb titanium alloy ingot with a diameter of 110 mm were obtained. The geometry of the two-phase liquidus–solidus zone, which determines the metal crystallization front, was determined. In the case of an electron beam heating power of 16 kW and a mass melting rate of 20 kg/h, such a crystallization front is formed, which provides a practically homogeneous structure of the metal ingot.

3. For the considered system of EBM process for Ti–6Al–7Nb titanium alloy, as a result of comparing the calculated metal crystallization profile in the ingot with a diameter of 110 mm with the crystallization profile of a molten ingot, it was proven that the laminar representation of hydrodynamic flows of the liquid metal in the ingot gives a result closer to the real profile than their turbulent representation.

4. Based on the calculated data, it was found that heat transfer in the liquid phase of the ingot is mainly predetermined by heat and mass transfer due to the movement of the molten metal, and the distribution of the electron beam power on the pool surface has a very significant effect on heat and mass transfer and on the depth of the melt pool.

5. It has been established that a flatter crystallization front of the metal ingot, which is desired, is formed at lower rates of pouring the melt into the mould and, accordingly, lower rates of ingot withdrawal.

REFERENCES

1. Tamayo José, A., Riascos Mateo, Vargas Carlos, A., Baena Libia, M. (2021) Additive manufacturing of Ti6Al4V alloy via electron beam melting for the development of implants for the biomedical industry. *Heliyon*, **7**, 1–26. DOI: DOI: https://doi.org/10.1016/j.heliyon.2021.e06892
2. Mahlobo Mandlenkosi, G.R., Chikosha Lethu, Olubambi Peter, A. (2022) Study of the corrosion properties of powder rolled Ti–6Al–4V alloy applied in the biomedical implants. *J. of Materials Research and Technology*, **18**, 3631–3639. DOI: https://doi.org/10.1016/j.jmrt.2022.04.004
3. Mamoun Fellah, Mohamed Labaïz, Omar Assala et al. (2014) Tribological behavior of Ti–6Al–4V and Ti–6Al–7Nb alloys for total hip prosthesis. *Advances in Tribology*, **July**, 1–13. DOI: https://doi.org/10.1155/2014/451387
4. Bartha, K., Zháňal, P., Stráský, J. et al. (2019) Lattice defects in severely deformed biomedical Ti–6Al–7Nb alloy and thermal stability of its ultra-fine grained microstructure. *J. of Alloys and Compounds*, **788**, 881–890. DOI: https://doi.org/10.1016/j.jallcom.2019.02.173
5. Bolzoni, L., Ruiz-Navas, E.M., Gordo, E. (2017) Evaluation of the mechanical properties of powder metallurgy Ti–6Al–7Nb alloy. *J. of the Mechanical Behavior of Biomedical Materials*, **67**, 110–116. DOI: https://doi.org/10.1016/j.jmbbm.2016.12.005
6. Sun, Y., Huang, B., Puleo, D.A. et al. (2016) Improved surface integrity from cryogenic machining of Ti–6Al–7Nb alloy for biomedical applications. *Procedia CIRP*, **45**, 63–66. DOI: https://doi.org/10.1016/j.procir.2016.02.362
7. Wei Guijiang, Tan Meiying, Attarilar Shokouh et al. (2023) An overview of surface modification, a way toward fabrication of nascent biomedical Ti–6Al–4V alloys. *J. of Materials Research and Technology*, **24**, 5896–5921. DOI: https://doi.org/10.1016/j.jmrt.2023.04.046
8. Oktikawati, A., Riastuti, R., Damisih, D. et al. (2024) Electrochemical characteristic and microstructure of Ti–6Al–7Nb alloy by centrifugal casting for orthopedic implant based on ageing time variations. *Eastern-European J. of Enterprise Technologies*, 2(**12**), 6–15. DOI: https://doi.org/10.15587/1729-4061.2024.302614
9. Hussain Syed Altaf, Manoj Panchal, Viswanath Allamraju K. et al. (2023) Optimization of wear behavior of heat-treated Ti–6Al–7Nb biomedical alloy by response surface methodology. *Environmental Research*, **231**, Pt 2, 116193. DOI: https://doi.org/10.1016/j.envres.2023.116193
10. Biswal, Smrutiranjan, Tripathy, S., Tripathy, D.K. (2024) Optimisation of PMEDM process parameters for Ti–6Al–7Nb biomedical material. *Materials Today: Proceedings*. DOI: https://doi.org/10.1016/j.matpr.2024.02.044

11. Cabrini, M., Carrozza, A., Lorenzi, S. et al. (2022) Influence of surface finishing and heat treatments on the corrosion resistance of LPBF-produced Ti–6Al–4V alloy for biomedical applications. *J. of Materials Processing Technology*, **308**, 117730. DOI: https://doi.org/10.1016/j.jmatprotec.2022.117730
12. Krivtsun, I., Rymar, S., Hubatiuk, R. et al. (2024) Construction of a mathematical model of turbulent heat and mass transfer processes for the case of electron beam melting of titanium alloy casts. *Eastern-European J. of Enterprise Technologies*, *Engineering Technological Systems*, 5(**1**). 110–126. DOI: https://doi.org/10.15587/1729-4061.2024.312561
13. Rubinetti, D., Weiss, D.A., Chaudhuri, A., Kraniotis, D. (2018) Modeling approach to facilitate thermal energy management in buildings with phase change materials. In: *Proc. of Conf. on Comsol 2018, Lausanne, Switzerland*, **7**. https://www.comsol.com/paper/modeling-approach-to-facilitate-thermal-energy-management-with-phase-change-mate-63481
14. Akhonin, S., Pikulin, O., Berezos, V. et al. (2022) Determining the structure and properties of heat-resistant titanium alloys VT3-1 and VT9 obtained by electron-beam melting. *Eastern-European J. of Enterprise Technologies*, 5(**12**), 6–12. DOI: https://doi.org/10.15587/1729-4061.2022.265014
15. Akhonin, S.V., Pikulin, O.M. (2019) Investigation of effect of electron beam surface treatment of titanium alloy ingots on structure and properties of melted metal. In: *Proc. of IOP Conf. on Series: Materials Science and Engineering*, 582 **(1)**, 012047. DOI: https://doi.org/10.1088/1757-899x/582/1/012047
16. Berezos, V.O., Akhonin, D.S. (2023) Electron beam melting of titanium alloys for medical purposes. *The Paton Welding J.*, **6**, 41–48. DOI: https://doi.org/10.37434/tpwj2023.06.06
17. Akhonin, S.V., Berezos, V.O., Bondar, O.I. et al. (2021) Mathematical modeling of hydrodynamic and thermal processes during the crystallization of titanium ingots EBM. *Suchasna Elektrometalurhiya*, **1**, 27–34 [in Ukrainian]. DOI: https://doi.org/10.37434/sem2021.01.03
18. Akhonin, S.V., Gorislavets, Yu.M., Gluhenkyi, A.I. et al. (2019) Modeling of hydrodynamic and thermal processes in the mould in cold-hearth electron beam melting. *Suchasna Elektrometalurhiya*, **4**, 9–17 [in Russian]. DOI: https://doi.org/10.15407/sem2019.04.02
19. Akhonin, S.V., Krivtsun, I.V., Berezos, V.O. et al. (2024) Mathematical modeling of heat and mass transfer processes of electron beam melting of ingots from high-strength titanium alloys. In: *Proc. of VII Inter. Conf. on Welding and Related Technologies, 7–10 October 2024, Yaremche, Ukraine. Kyiv*, 119–124, Kyiv, International Association «Welding». DOI: https://doi.org/10.1201/9781003518518-25
20. Ben-David, O., Levy, A., Mikhailovich, B., Azulay, A. (2013) 3D numerical and experimental study of gallium melting in a rectangular container. *Inter. J. of Heat Mass Transfer*, **67**, 260–271. DOI: http://dx.doi.org/10.1016/j.ijheatmasstransfer.2013.07.058
21. Heat Transfer Module User's Guide. Version: Comsol 5.4. http://www.comsol.com
22. Versteeg, H.K., Malalasekera, W. (2007) *An introduction to computational fluid dynamics. The finite volume method*. Harlow, Pearson Prentice Hall.
23. Avnaim, M.H., Levy, A., Mikhailovich, B. et al. (2016) Comparison of three-dimensional multidomain and single-domain models for the horizontal solidification problem. *J. of Heat Transfer*, 138(**11**), 112301-1–112301-11. DOI: https://doi.org/10.1115/1.4033700
24. Truong Van-Doi, Yong-Taek Hyun, Jong Woo Won et al. (2022) Numerical simulation of the effects of scanning strategies on the aluminum evaporation of titanium alloy in the electron beam cold hearth melting process. *Materials,* **15**. DOI: https://doi.org/10.3390/ma15030820
25. Yao Lu, Maijer Daan M., Cockcroft Steve L. et al. (2018) Quantification of heat transfer phenomena within the melt pool during the plasma arc remelting of titanium alloys. *Inter. J. of Heat and Mass Transfer*., **126**, 1123–1133. DOI: https://doi.org/10.1016/j.ijheatmasstransfer.2018.06.051
26. Belyaev, N.M. (1989) *Fundamentals of Heat Transfer*. Kyiv, Vyshcha Shkola [in Russian].
27. Mills, K. (2002) *Recommended values of thermophysical properties for selected commercial alloys*. Woodhead publishing Limited.
28. Efimov, A.I., Belorukova, L.P., Vasilkova, I.V., Chechev, V.P. (1983) *Properties of inorganic compounds. Directory*. Leningrad, Khimiya.
29. Langmuir, I. (1913) The vapor pressure of metallic tungsten. *Physical Review*, 2**(5)**, 329–342. DOI: https://doi.org/10.1103/physrev.2.329
30. Berezos, V.O., Akhonin, D.S. (2023) Electron beam melting of titanium alloys for medical purposes. *The Paton Welding J.*, **6**, 41–48. DOI: https://doi.org/10.37434/tpwj2023.06.06

ORCID
I.V. Krivtsun: 0000-0001-9818-3383,
S.V. Rymar: 0000-0003-0490-4608,
R.S. Gubatyuk: 0000-0002-0851-743X,
V.O. Berezos: 0000-0002-5026-7366,
D.S. Akhonin: 0009-0000-2054-4054,
R.V. Selin: 0000-0002-2990-1131

CONFLICT OF INTEREST
The Authors declare no conflict of interest

CORRESPONDING AUTHOR
S.V. Rymar
E.O. Paton Electric Welding Institute of the NASU
11 Kazymyr Malevych Str., 03150, Kyiv, Ukraine.
E-mail: elmag@paton.kiev.ua

SUGGESTED CITATION
I.V. Krivtsun, S.V. Rymar, R.S. Gubatyuk, V.O. Berezos, D.S. Akhonin, R.V. Selin (2025) Mathematical modeling of heat and mass transfer processes during electron beam melting of Ti–6Al–Nb titanium alloy ingots. *The Paton Welding J.*, **9**, 18–32.
DOI: https://doi.org/10.37434/tpwj2025.09.03

JOURNAL HOME PAGE
https://patonpublishinghouse.com/eng/journals/tpwj

Received: 24.06.2025
Received in revised form: 12.08.2025
Accepted: 18.09.2025